NANO LETTERS

Letter

pubs.acs.org/NanoLett

$In_xGa_{1-x}As$ Nanowire Growth on Graphene: van der Waals Epitaxy Induced Phase Segregation

Parsian K. Mohseni, Ashkan Behnam, Joshua D. Wood, Christopher D. English, Joseph W. Lyding, Eric Pop, and Xiuling Li*

Department of Electrical and Computer Engineering, Micro and Nanotechnology Laboratory, Beckman Institute for Advanced Science and Technology, University of Illinois at Urbana−Champaign, Urbana, Illinois 61801, United States

Supporting Information

ABSTRACT: The growth of high-density arrays of vertically oriented, single crystalline InAs NWs on graphene surfaces are realized through the van der Waals (vdW) epitaxy mechanism by metalorganic chemical vapor deposition (MOCVD). However, the growth of InGaAs NWs on graphene results in spontaneous phase separation starting from the beginning of growth, yielding a well-defined InAs−$In_xGa_{1-x}As$ ($0.2 < x < 1$) core−shell structure. The core−shell structure then terminates abruptly after about 2 μm in height, and axial growth of uniform composition $In_xGa_{1-x}As$ takes place without a change in the NW diameter. The $In_xGa_{1-x}As$ shell composition changes as a function of indium flow, but the core and shell thicknesses and the onset of nonsegregated $In_xGa_{1-x}As$ axial segment are independent of indium composition. In contrast, no InGaAs phase segregation has been observed when growing on MoS_2, another two-dimensional (2D) layered material, or via the Au-assisted vapor−liquid−solid (VLS) mechanism on graphene. This spontaneous phase segregation phenomenon is elucidated as a special case of van der Waals epitaxy on 2D sheets. Considering the near lattice matched registry between InAs and graphene, InGaAs is forced to self-organize into InAs core and InGaAs shell segments since the lack of dangling bonds on graphene does not allow strain sharing through elastic deformation between InGaAs and graphene.

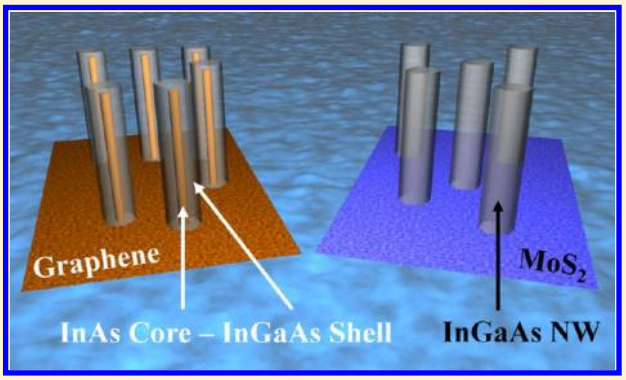

KEYWORDS: *van der Waals epitaxy, nanowire, MOCVD, InGaAs, InAs, phase segregation, phase separation, graphene*

Heteroepitaxy offers a route toward unification of the distinct characteristics of dissimilar materials within a monolithic structure that is otherwise not found in nature. To date, one of the most exalted advantages offered by semiconductor nanowires (NWs) is their ability to retain their crystalline quality under highly lattice-mismatched heteroepitaxial growth conditions.[1−4] The capacity for the relaxation of heterointerface-induced strain, offered by NW geometries, prevents the formation of dislocations that plague conventional highly mismatched bulk heterostructures.[5−7] Based on this principle, already demonstrated NW-based devices such as lasers,[8] light-emitting diodes,[9] and photovoltaic solar cells[10,11] composed of compound semiconductors can be integrated with more technologically mature platforms such as Si[12−16] and more economically desirable substrate materials like glass.[17]

Of particular interest for a novel class of optoelectronic devices is the growth of semiconductor nanostructures on mechanically flexible and electrically conductive materials. To this end, Au-assisted growth of GaAs NWs on composite films of single-walled carbon-nanotubes[18,19] and Si NWs on stainless steel foils[20] have been demonstrated in recent years. In these cases, the resultant NWs are oriented at a wide distribution of angles with respect to the surface normal, due to a lack of long-range atomic periodicity presented by the flexible substrates. In contrast, graphene, having a two-dimensional (2D) planar configuration of sp^2-bonded carbon atoms, possesses the required combination of long-range atomic periodicity, mechanical strength and flexibility, high electrical conductivity, and optical transparency[21−23] to serve as an ideal substrate for vertically aligned semiconductor NW growth for flexible optoelectronics.

Recently, growths of various functional materials on graphene layers have been reported, including thin films of MoS_2[24] and Cu-doped SnS,[25] as well as GaAs,[26] ZnO,[27] and InAs[28] one-dimensional (1D) nanostructures. Particularly relevant to the current work is the latter study carried out by Hong et al.,[28] wherein orientational control of InAs NWs, formed through van der Waals epitaxy (vdW Epi) by metal−organic chemical vapor deposition (MOCVD), was explored as a function of thickness and surface roughness of graphene-based substrates. vdW Epi refers to a particular crystal growth scenario wherein an epi-layer is formed on a substrate having no dangling bonds.[29] In such a scenario, the epi-layer/substrate

Received: December 10, 2012
Revised: February 11, 2013

   dx.doi.org/10.1021/nl304569d | *Nano Lett.* XXXX, XXX, XXX−XXX

interface is maintained purely through van der Waals interactions, allowing for dislocation-free incommensurate growth.[29]

Although the material combination of InAs and graphene through vdW Epi has been previously reported, the nature of epitaxial registry in such material systems and the growth of ternary compound semiconductor heterostructures on graphene remain unexplored. In this work, we present a self-organized method for the formation of coaxially heterostructured InAs/$In_xGa_{1-x}As$ NWs, over a wide tunable ternary compositional range, on large-area graphene substrates. We demonstrate that the self-organization phenomenon observed is unique to the $In_xGa_{1-x}As$ NW growth on graphene, as otherwise identical growths on Si substrates and MoS_2 2D sheets yield only stoichiometrically single phase InGaAs NWs. Moreover, we show that phase segregation does not occur for Au-assisted InGaAs NW growth on the same kind of graphene substrates. Therefore, we conclude that the preferential phase segregation is the distinctive outcome of vdW Epi of a ternary compound, in which a binary component is close to lattice matched with the 2D substrate. Such heterogeneous nanostructures can be exploited for the fabrication of a novel class of functional hybrid materials for use in flexible optoelectronic device applications.

Growth of NWs was performed in an AIXTRON 200/4 MOCVD reactor through a seed-free, self-assembly mechanism. Trimethyl-indium [TMI, $(CH_3)_3In$], trimethyl-gallium [TMG, $(CH_3)_3Ga$], and arsine (AsH3) were used as the precursors for In, Ga, and As, respectively. For this study, six NW sample groups with different compositions, henceforth referred to as Groups 1−6, were investigated. The growth conditions used for each sample group are summarized in Table 1, where $\xi = \chi_{TMI}/(\chi_{TMI} + \chi_{TMG})$, and χ_{TMI} and χ_{TMG} represent TMI and TMG molar flow rates, respectively. Growth times were 10 min unless otherwise indicated. Graphene growth was performed by chemical vapor deposition (CVD) on Cu (1 mil and 5 mil thickness, 99.8% purity) with a process discussed previously.[30,31] Continuous sheets of monolayer graphene were transferred to 90 nm SiO_2/n++ Si by poly(methyl methacrylate) (PMMA).[31,32] Discontinuous graphene samples were also CVD-grown and transferred to SiO_2 by a polybisphenol A carbonate (PC) transfer method.[33] Unless otherwise indicated, the graphene film is single layer; growth on multilayer graphene was also examined, and no significant difference was found. Details of the NW growth and graphene preparation are described in the Experimental Methods.

Table 1. Growth Conditions and Resultant $In_xGa_{1-x}As$ NW Composition for Various Sample Groups

NW group	growth temperature (°C)	growth duration (min)	gas phase In/(In+Ga) molar flow ratio, ξ	NW $In_xGa_{1-x}As$ Phase composition, x[a]
1	550	10	1	1
2	570	10	0.65	0.74
3	570	10	0.59	0.56
4	570	10	0.52	0.39
5	570	10	0.42	0.29
6	570	10	0.27	0.21

[a]As determined through XRD analysis.

First, we demonstrate the growth of high density InAs NW arrays on graphene substrates. Figure 1a shows a dense array of vertically oriented binary InAs NWs, with an average diameter of ∼87 nm (standard deviation of 17 nm) and average lengths of ∼3.4 μm (standard deviation of 0.15 μm). The density of these NWs is estimated to be 7×10^8 cm^{-2}, which is ∼7× higher as compared to that of previously reported InAs NWs grown on graphene under comparable conditions.[28] We attribute the vertical alignment of NWs to the pseudocoherent relationship between zincblende (Zb) InAs and the graphene surface.[28] This is because the lattice constant of Zb InAs along the ⟨110⟩ direction corresponds to the carbon−carbon bond length of graphene (1.41 Å) by a multiple of 6.03. Thus, nearly lattice-matched growth of InAs crystals along the ⟨111⟩ direction can be expected on (0001) graphene surfaces. We have found that such NW assembly depends strongly upon growth temperature. Below 520 °C, NW formation is fully quenched, and only parasitic island growth persists. On the other hand, growth temperatures above 580 °C result in the decrease of NW density, likely due to a reduction of nucleation sites resulting from the enhanced desorption of growth species (Supporting Information, Figure S1). It should be noted that nonvertical NW growth has been observed to occur on the parasitic islands and that island growth is predominant along line defects present within graphene layers as well as at the edges of the graphene sheets (Supporting Information, Figure S2). A representative high-resolution transmission electron microscopy (HR-TEM) image obtained from the center of an InAs NW is shown in Figure 1b. As anticipated,[28] the InAs NWs grown on graphene exhibit a Zb crystal structure with growth along the ⟨111⟩ direction. A high density of stacking faults are observed, characterized as twin planes, similar to what had been previously reported for seed-free, MOCVD-grown, InAs nanostructures.[14,28] All InAs NWs show uniform diameters throughout their lengths, with {−110} terminated sidewall facets. Some NWs exhibit a slightly truncated sidewall profile at the NW tip (∼4 nm long segment) (Supporting Information, Figure S3).

Of further interest is the degree of selectivity offered by graphene films for NW growth. Figure 2 shows a tilted-view SEM image of InAs NWs grown on a discontinuous graphene layer, containing numerous regions of pristine graphene islands, among an otherwise graphene-free, SiO_2 substrate. The graphene islands have dimensions on the order of tens of micrometers, separated by comparable lengths. The locations of bare SiO_2 and graphene-encapsulated SiO_2 were confirmed prior to growth through AFM and Raman spectroscopy characterization (Supporting Information, Figure S4). The inset of Figure 2 shows the post-growth border (marked by a dotted line) formed by a graphene island and the SiO_2 substrate. A clear areal selectivity is observed, insofar as NW formation is exclusively limited to the graphene-covered regions. In contrast, polycrystalline island growth occurs on the exposed oxide regions. Figure 2 demonstrates unambiguously that vdW Epi of vertical InAs NWs by MOCVD is selective to the graphene surface. Such selectivity can be exploited for the growth of patterned NW arrays by pregrowth lithographic patterning of graphene sheets. It should also be noted that the growth of such seed-free NWs places no adverse influence upon the structural quality of the graphene films, as determined through Raman scattering spectroscopy (Supporting Information, Figure S5). We anticipate, therefore, that device applications employing hybrid nanomaterials of this nature may benefit from the dual role of graphene as both a

dx.doi.org/10.1021/nl304569d | Nano Lett. XXXX, XXX, XXX−XXX

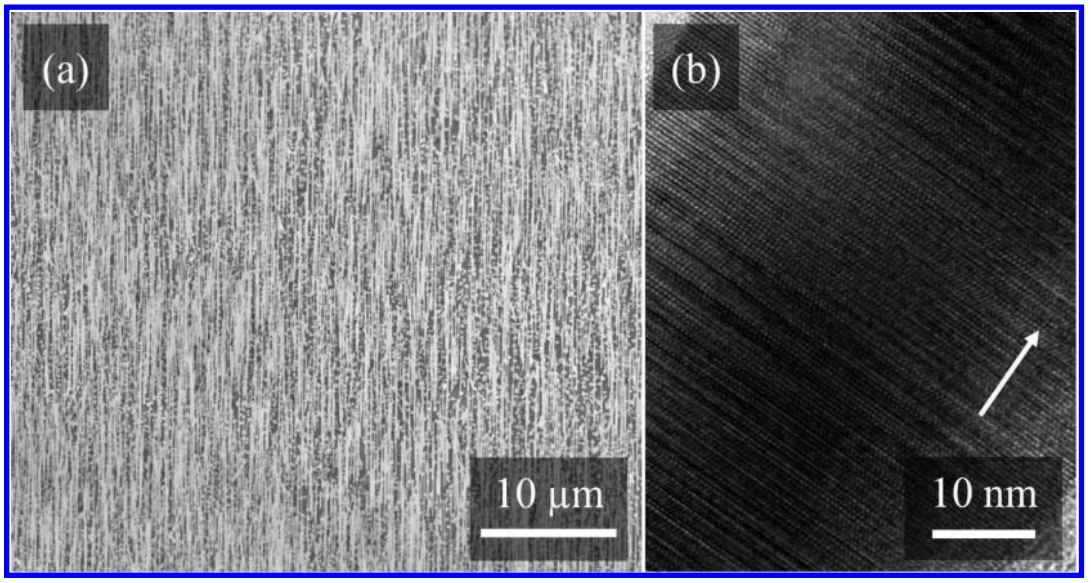

Figure 1. High density vertical InAs NW growth on graphene. (a) 45° tilted-view SEM image of as-grown InAs NWs (Group 1) on a large area (1 × 1 cm^2), defect-free graphene substrate with average NW density of 7 × 10^8 cm^{-2}. (b) HR-TEM image of an InAs NW, showing a high density of stacking faults along the NW. The white arrow points toward the NW tip.

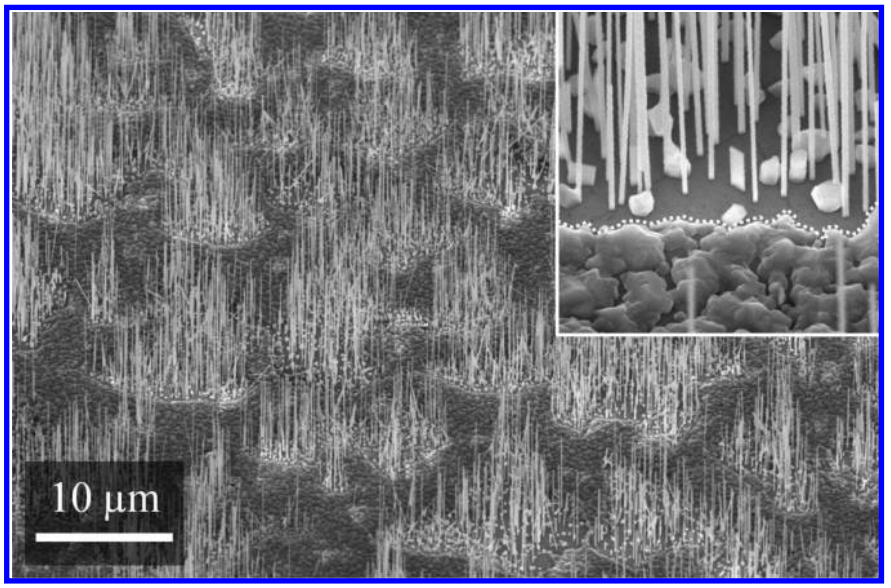

Figure 2. Selective-area vdW Epi of InAs NWs on graphene. 45° tilted-view SEM image of InAs NWs grown on a discontinuous graphene film. NW growth occurs exclusively on the graphene islands. The inset shows a higher magnification image of the graphene (top)/SiO_2 (bottom) boundary, delineated by the white dotted line.

substrate for epitaxial growth and as an optically transparent electrode.

In addition to InAs NW growth on graphene substrates, we have systematically studied ternary $In_xGa_{1-x}As$ NW growth over a wide composition range ($0.2 < \xi < 1$) on continuous graphene films, as summarized in Table 1. To the best of our knowledge, the current study represents the first demonstration of growth of ternary $In_xGa_{1-x}As$ NWs on graphene substrates. The anticipated mismatch between $In_xGa_{1-x}As$ and graphene is only ∼0.5% for $x = 1$ (InAs)[26,28] and ∼5.65% for $x \sim 0.2$. Figure 3a shows a representative SEM image of $In_xGa_{1-x}As$ NWs (Group 4 NWs, $\xi = 0.52$) grown over large areas under similar growth condition as that of InAs NWs. The inset shows a high magnification image of the same sample. SEM images for all other compositions can be found in the Supporting Information (Figure S6). In comparison to pure binary InAs NWs, the average diameters of the $In_xGa_{1-x}As$ NWs increase from 87 ± 17 nm to 132 ± 24 nm, independent of indium composition. Although all $In_xGa_{1-x}As$ NWs investigated here are vertically aligned with respect to the graphene surface, roughly 40% exhibit a curved morphology near the NW top. Curved morphologies had been previously observed in the case of Au-assisted $In_xGa_{1-x}As$ NWs[34,35] and for seed-free $In_xGa_{1-x}As$ NWs grown on Si (111),[14] where the nature of bending had been attributed to strain induced by composition inhomogeneity. The NW curvature observed here appears to increase with increasing Ga%, implying that more strain is present in the NW as the composition deviates from InAs.

X-ray diffraction (XRD) measurements were carried out for NW composition characterization. Figure 3b shows the XRD

dx.doi.org/10.1021/nl304569d | Nano Lett. XXXX, XXX, XXX−XXX

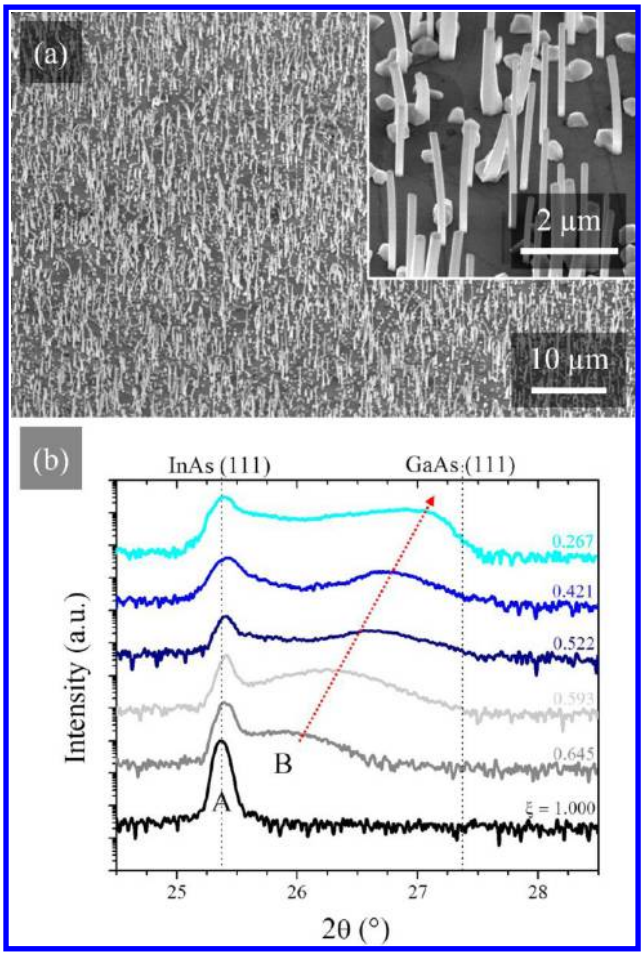

Figure 3. $In_xGa_{1-x}As$ NW growth on graphene. (a) Tilted view of Group 4 $In_xGa_{1-x}As$ NWs (ξ = 0.52), with a higher magnification image shown in the inset. (b) Normalized XRD rocking curves plotted on a logarithmic scale, obtained from Group 1−6 NWs (from bottom to top). Each curve is labeled with the associated gas phase In/(In + Ga) molar flow ratio, ξ, as summarized in Table 1. Vertical dashed lines indicate the expected positions of InAs (111) and GaAs (111) diffraction signals. Peaks labeled A and B show the positions of the InAs and InGaAs peaks, respectively. The dashed orange line serves as a guide to the eye, tracing the evolution of the characteristic InGaAs signal with decreasing ξ.

rocking curves for all NW groups, with intensity plotted on a logarithmic scale and offset vertically for clarity. The rocking curve associated with each NW group is labeled with the gas phase molar flow ratio of group-III precursors, ξ, employed during growth. Vertical dashed lines located at 25.4° and 27.3° denote the peak positions associated with diffraction from InAs (111) and GaAs (111) planes, respectively.[36]

Two key aspects of the XRD results shown in Figure 3b require further discussion. First, the presence of the InAs (111) peak, labeled as peak "A", is observed for all NW groups. From the presence of peak A, it is understood that all NW samples possess a phase consistent with (111) oriented crystalline InAs. Second, with the exception of group A NWs (purely InAs), all other NW groups exhibit an additional peak, labeled as peak "B", situated between the position of the signals expected from InAs (111) and GaAs (111). Peak B is, therefore, representative of diffraction from InGaAs (111) planes. The position of peak B increases monotonically toward the GaAs (111) position with decreasing values of gas phase In/(In + Ga) molar flow ratio, ξ, as represented by the orange dashed arrow. Neglecting the Poisson ratio and assuming complete relaxation of the NW lattice, the In-composition of all $In_xGa_{1-x}As$ samples can be derived from the position of peak B, as summarized in Table 1. The broadening of the InGaAs peaks could be attributed to compositional nonuniformity among the large collection of individual NWs, as well as island structures.

The XRD results indicate that all ternary $In_xGa_{1-x}As$ NWs over the wide compositional range studied have two distinct phases; namely, an InAs phase and an InGaAs phase. The composition of the InGaAs phase changes as a function of gas phase In/(In+Ga) molar flow ratio, ξ. Given that all NW samples were individually grown under constant TMI to TMG ratios in a single step, the presence of two distinct phases is unexpected. To gain further insight into the phase segregation mechanism, scanning transmission electron microscopy (STEM) analysis was carried out on individual NWs from all $In_xGa_{1-x}As$ sample groups.

Through high-angle annular dark-field (HAADF) imaging, whereby contrast variations reflect compositional differences due to a high degree of *Z*-contrast, two distinct phases are identified in individual $In_xGa_{1-x}As$ NWs. Figure 4a shows an HAADF image obtained from a region near the base of a NW from a Group 4 sample (ξ = 0.52). Here, two distinct segments can be observed: a central region of bright contrast, encapsulated by a peripheral region of relatively darker contrast. Therefore, a definitive core−shell heterostructure is found. Shown in Figure 4b is the energy dispersive X-ray (EDX) linescan results obtained across the NW as indicated by the dashed line in Figure 4a. Here, elemental counts of In, Ga, and As are plotted as a function of radial position as black (square), red (circular), and blue (triangular) data points, respectively. Counts of elemental As increase toward the center region, in comparison to the peripheral regions, representative of the radial thickness profile of a cylindrical wire shape. At the center of the NW, counts of elemental In increase while the elemental Ga counts decrease, confirming the core−shell composition changes. Combining with the XRD data in Figure 3, the HAADF contrast variations and the radial EDX linescan analysis are consistent with a NW architecture wherein an InAs core is surrounded by an InGaAs shell. Note that the presence of a finite Ga signal in the center is due to the presence of elemental Ga in the shell segment.

An HAADF image obtained from roughly the longitudinal center of the same NW is shown in Figure 4c, wherein the white arrow points toward the NW tip. Here, two features should be highlighted. First, closer to the base (left side) the same radial heterostructure as shown in Figure 4a can be distinguished. Second, moving toward the NW tip, a slight contrast variation can be observed in the axial direction, corresponding to a transition to darker contrast closer to the tip (right side). Based on the axial EDX linescan shown in Figure 4d and obtained along the dashed line in Figure 4c, the transition toward the region of darker contrast closer to the NW tip corresponds to a point where a gradual decrease in elemental In and increase in elemental Ga simultaneously occur. This transition represents a compositional variance from InAs to InGaAs along the axial growth direction. Therefore, the formation of the InAs core becomes quenched while InGaAs axial growth persists, resulting in a single phase InGaAs shell encapsulating the InAs core from all sides. The same structural profiles were observed for all other sample groups. It should be noted that the compositions of the $In_xGa_{1-x}As$ phases obtained

dx.doi.org/10.1021/nl304569d | *Nano Lett.* XXXX, XXX, XXX−XXX

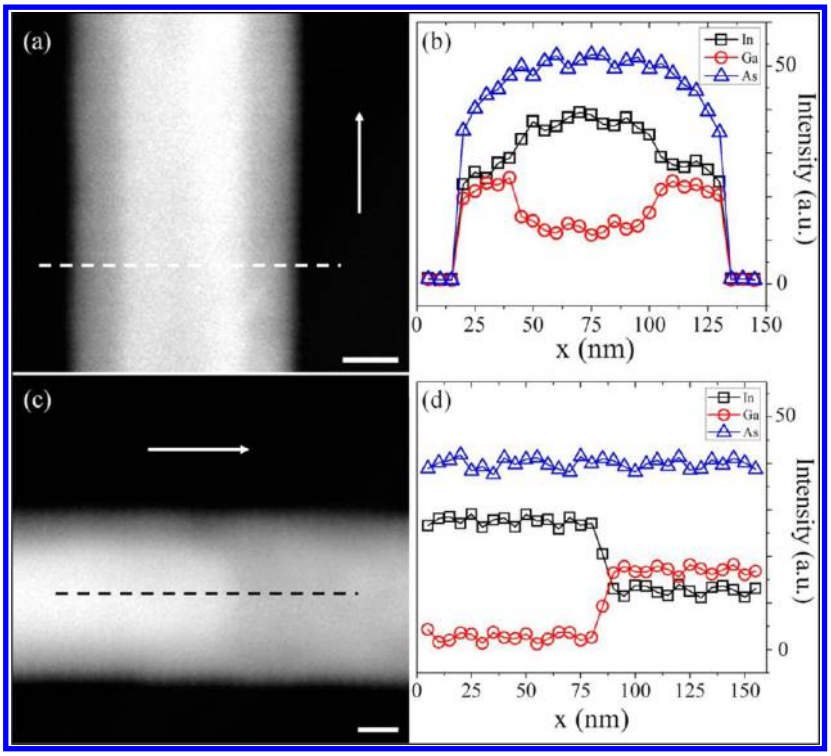

Figure 4. Phase-separated InGaAs NW. (a) HAADF image showing a region near the base of a Group 4 NW. The white dashed line shows the position, *x*, along which the radial EDX linescan shown in (b) was obtained. (c) HAADF image from the central portion of the same NW as in (a). The black dashed line shows the position, *x*, where the axial EDX linescan shown in (d) was collected. The white arrows in (a) and (c) point toward the NW tip; the scale bars represent a 25 nm length. Black (squares), red (circles), and blue (triangles) data points represent detected counts of elemental In, Ga, and As, respectively.

from XRD analysis, as specified in Table 1, are in agreement within <5% as compared to composition values obtained through EDS point measurements.

Although compositional inhomogeneity[37] and phase segregation[38] in InGaAs nanowires have been recently reported, the current study is the first example of a material system wherein an inert, 2D substrate directly influences the compositional phase of the epi-layers. To more accurately access the evolution of the observed segregation effect, the early stages of NW growth (2 and 5 min growth time) are examined (compared to a growth period of 10 min for all other NW groups discussed thus far). Figures S7a–c show tilted-view SEM images of Group 4 NWs after 2, 5, and 10 min growth periods, respectively. The mean NW length and diameter values as a function of growth duration are quantified in Figure S7d of the Supporting Information. Two key features arise from the growth-evolution study. First, as the NW lengths increase nearly linearly with growth time, the NW diameters remain constant within one standard deviation. Through HAADF analysis (Supporting Information, Figure S8), it is determined that the average thickness of phase segregated InAs core segments and InGaAs shell segments are fixed during the early stages of growth. For all NWs analyzed, shell thickness values ranging between 19 and 25 nm are measured, regardless of the total growth duration and composition. Therefore, we hypothesize that radial material segregation occurs in the early stages of growth, possibly at time zero, and axial propagation of growth fronts advance nearly in tandem for both core and shell segments. How close to time zero will have to be determined by higher time-resolution snap shots of the initial growth and in situ TEM analysis. Second, for growth times up to 5 min, NWs do not show curved or bent morphologies. No evidence for single phase axial InGaAs NW growth is found by HAADF. This confirms that the curved NW morphology is a direct result of strain induced bending in the axial single phase InGaAs segment. Based on the NW axial growth rate, the onset of the single phase InGaAs NW growth occurs right after 5 min. Beyond the 5 min growth period, axial extension of the InAs core segment is quenched, such that the InGaAs shell segment envelopes the core and extends the NW height, as a single-stoichiometry InGaAs phase. Remarkably, there is no detectible change in diameter or composition and the axial phase change onset position (~2 μm from the NW/graphene interface) is independent of InGaAs composition. The mechanism of the axial growth termination of InAs core segments is unclear at this point but should be related to the van der Waals interaction of the InGaAs NW and graphene substrate, since the transition point appears to be independent of InGaAs composition. Future investigations, including growths on h-BN sheets to evaluate the effect of the van der Waals attraction, growth interruption before the transition to evaluate surface preparation effects, as well as theoretical modeling of the energetics of the hybrid structure, will help provide more insight on the mechanism of this phenomenon.

We believe that the radial heterostructure self-organization process is a direct consequence of the commensurate relationship of InAs lattice parameter with the nearest-neighbor carbon atom spacing of graphene.[28] As strain sharing is not permitted in the case of growth on an inert substrate, the binary InAs component of ternary InGaAs preferentially self-assembles as the core segment. To further evaluate this hypothesis, growth of InGaAs NWs on exfoliated MoS_2 layers, deposited on SiO_2

dx.doi.org/10.1021/nl304569d | *Nano Lett.* XXXX, XXX, XXX–XXX

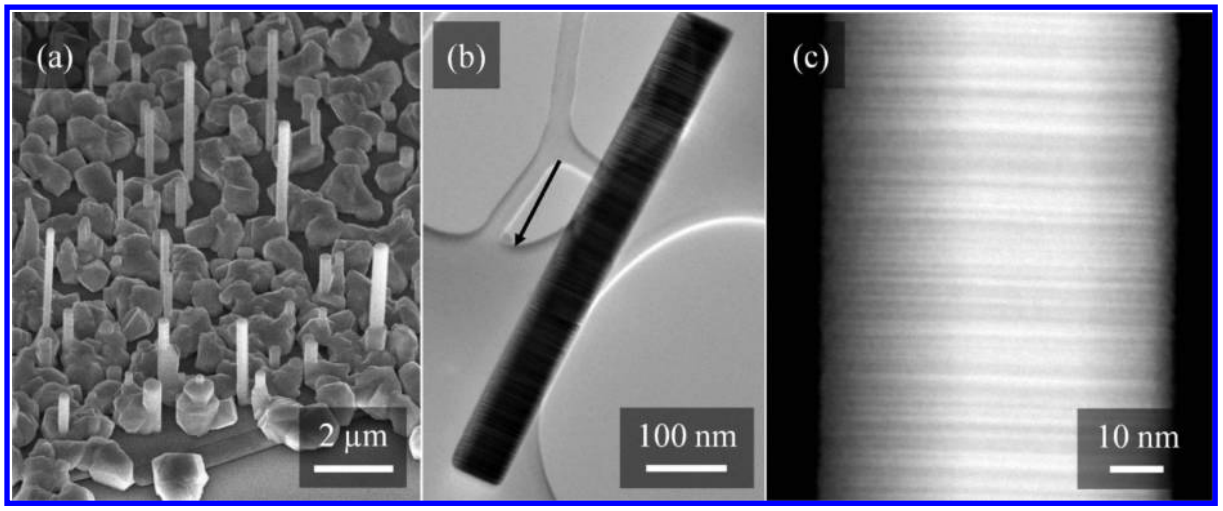

Figure 5. InGaAs NWs on MoS_2 substrates. (a) 45° tilted-view SEM image of as-grown InGaAs NWs (ξ = 0.52) on an exfoliated MoS_2 substrate. (b) Bright-field TEM image of an InGaAs NW removed from the MoS_2 growth surface. The black arrow indicates the growth direction, as discerned from the slightly truncated tip structure. (c) HAADF-STEM images obtained from the midsection of the same NW shown in (b).

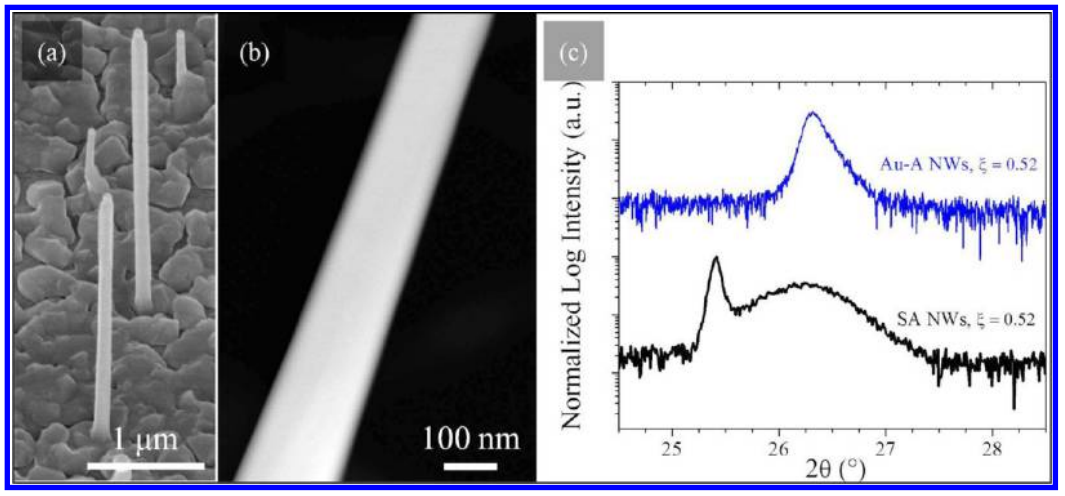

Figure 6. Au-assisted InGaAs NWs grown on graphene. (a) 45° tilted-view SEM image of as-grown Au-assisted InGaAs NWs on a graphene substrate. Au particles are visible at the NW tips, indicating VLS-type growth. (b) HAADF-STEM image obtained from the midsection of an Au-assisted InGaAs NW, showing no evidence of radial or axial phase segregation. (c) XRD rocking curves obtained from as-grown Au-assisted (Au-A, blue curve) and self-assembled (SA, black curve) $In_xGa_{1-x}As$ NW samples grown on graphene substrates (ξ = 0.52, for both cases).

surfaces, has been performed. MoS_2 was chosen as an alternative growth surfaces based upon the following two criteria: (1) as in the case of graphene, MoS_2 is a planar (2D) material capable of accommodating vdW Epi growth;[24] and (2) MoS_2 has a lattice parameter of 3.16 Å (larger than graphene by approximately 28%), offering an alternative surface atomic configuration with respect to graphene. As such, the role of atomic registry in pseudo-lattice-matched InAs−graphene and lattice-mismatched InAs−MoS_2 systems can be distinguished. InGaAs NW growth on exfoliated MoS_2 flakes was carried out under identical MOCVD growth conditions to that of the Group 4 NW sample (ξ = 0.52) described above. Figure 5a shows a 45° tilted-view SEM image of InGaAs NWs on MoS_2 islands situated on a SiO_2 background. To our knowledge, this is the first demonstration of this particular material combination and exploration of this hybrid system. Although the growth parameter space is not optimized yet, as can be seen in Figure 5a, vertical NW growth is achieved with heights up to 5 μm and diameters in the 75−520 nm range. Despite the relatively high degree of parasitic island growth, NW bases can be seen to stem directly from the surface of the MoS_2 substrates. The sparse nature of these NWs prevents the acquisition of meaningful XRD data from this sample. As such, compositional characterization was carried out exclusively through STEM and EDX experiments. Figure 5b shows a bright-field TEM image obtained from a single InGaAs NWs removed from the MoS_2 surface via ultrasonication. Additional diffraction pattern analysis (not shown) from the same NW demonstrates a predominant Zb crystal structure with a high density of stacking faults, consistent with structural analysis performed on Group 4 NWs. Figure 5c shows an HAADF image obtained from the central segment of the same NW. Here, no spatially distinct compositional variances are discerned, in contrast to all $In_xGa_{1-x}As$ NWs grown on graphene substrates. The slight contrast increase toward the center of the NW shown in Figure 5c is attributed to the increased thickness of the sample near its center. Furthermore, through EDX point analysis from various regions along numerous sets of $In_xGa_{1-x}As$ NWs grown on MoS_2, it is established that these nanowires are homogeneous in

dx.doi.org/10.1021/nl304569d | Nano Lett. XXXX, XXX, XXX−XXX

composition within the resolution of EDX measurement ($x \sim 0.47-0.5$ for Group 4), and do not consist of compositionally distinct $In_xGa_{1-x}As$ phases in either the axial or radial directions. Therefore, it is concluded that phase segregation, as observed in the case of growth on graphene, does not occur in InGaAs NWs grown on MoS_2. This implies that the absence of atomic registry between substrate and epi-layer forces the growth of single compositional phase InGaAs NWs on 2D materials, which is the expected outcome of the vdW Epi growth mechanism.

In addition, we have examined Au-assisted VLS growth of InAs and InGaAs NWs on graphene for spontaneous phase segregation. Growths of Au-assisted NWs on graphene are performed at the 450−470 °C temperature range (other growth conditions were the same as seed-free InAs and InGaAs NW growths on graphene), such that the formation of Au-free NWs is effectively suppressed. Through this approach, growth of vertically oriented Au-assisted InGaAs NWs (ξ = 0.52, for comparison with Group 4 NWs) on graphene substrates is realized, as shown in Figure 6a. Analysis of the Au-assisted InGaAs NW samples via STEM, shown in Figure 6b, reveals no evidence of material phase segregation. An XRD rocking curve obtained from the same as-grown sample of Au-assisted InGaAs NWs is shown in Figure 6c and compared to that of the Group 4 NWs (ξ = 0.52) grown on graphene. The absence of a diffraction signal from purely InAs (111) planes in the XRD rocking curves of an ensemble of Au-assisted InGaAs NWs shows that single phase growth can be suitably realized when self-assembled (SA) NW growth is restricted. All of the above control experiments indicate that segregation of InAs-core and InGaAs-shell segments during the growth of InGaAs NWs on graphene substrates is a phenomenon that only occurs in the unique vdW Epi scenario wherein lattice registry exists between a 2D substrate and a binary component of an otherwise ternary material.

In summary, we have grown high-density vertical InAs NW arrays and self-organized core−shell heterostructured InAs−InGaAs NWs through a seed-free vdW Epi approach on graphene films by MOCVD. Anisotropic crystal growth, leading to the formation of ideal NW structures prevails on pristine graphene regions, while parasitic growth occurs along linear-defects and edges of the graphene substrates. Growth of NWs causes no detectable adverse influence upon the quality of the graphene films. An epitaxial selectivity has been observed, allowing NW growth to pursue exclusively on graphene-coated SiO_2, in comparison to bare oxide surfaces. In the case of InGaAs on graphene growth, we have uncovered a unique phase segregation phenomenon, causing the self-organization of coaxial heterostructures into InAs-core and InGaAs-shell segments. We have attributed this self-assembly mechanism to the commensurate relationship between the InAs crystal structure and the 2D graphene lattice and the lack of strain accommodation of graphene to InGaAs due to the weak vdW interaction. In other words, no dangling bonds are available on graphene to form covalent bonds that can be stretched to accommodate the tensile strain in InGaAs, if it were to stay as one phase epitaxially. Future efforts will be focused toward the mitigation of stacking faults in these NWs and the exploration of potential phase segregation effects in vdW Epi of other ternary (such as InAsP) NWs grown on graphene or other 2D films. Such material combinations of compound III−V semiconductors and monolayer graphene films can lead to the demonstration of novel device applications in flexible electronics and optoelectronics.

Experimental Methods. Using a 1-in. Atomate CVD growth furnace, Alfa Aesar Cu foils (1 mil, 99.8% purity, and 5 mil, 99.8% purity) were annealed in Ar and H_2 gases for 25 min at 1000 °C. Graphene was grown on these foils at 75 sccm of CH_4 and 50 sccm of H_2, employing a base pressure of 500 mTorr. This resulted primarily in monolayer graphene growth on both sides of the Cu foils. The graphene was transferred off the Cu growth substrates using two methods.

The first method used a thick layer of poly(methyl methacrylate) (PMMA) on a 1 mil Cu growth foil, coating one graphene/Cu side with ∼250 nm of PMMA (a PMMA bilayer using 495K and 950K molecular weights). The graphene on the other Cu side was removed by a 20 sccm O_2 plasma reactive ion etch (RIE) for 30 s (in a PlasmaLab Master/Slave Dual-Chamber Reactive Ion Etcher). The Cu foil was then etched overnight in aqueous $FeCl_3$ (Transene, CE-100), leaving the graphene supported by the PMMA floating on the surface of the solution. The PMMA + graphene bilayer film was transferred via a piranha-cleaned glass slide to a deionized water bath for 15 min. The film was then transferred into a modified SC-2 (20:1:1 $H_2O/H_2O_2/HCl$) bath for 10 min followed by a 10 min modified SC-1 (20:1:1 $H_2O/H_2O_2/NH_4OH$) bath.[32] Finally, the film was rinsed again in deionized water before being transferred to a SiO_2 (90 nm) on Si substrate (p+ doped, <5 mΩ·cm resistivity). These samples were air-dried for ∼10 min and then further dried with ∼10 min of 150 °C heating in air. The PMMA is removed using a 1:1 mixture of methylene chloride and methanol for ∼15 min, and the samples were degreased and dried in N_2. No Ar/H_2 anneal was performed.

The second method used a thin layer of polybisphenol A carbonate (PC) to transfer the graphene off the Cu growth surface (5 mil Cu). The 5 mil Cu foil produced incomplete graphene coverage during growth from substrate effects.[30] PC was freshly mixed in chloroform at 1.2% by weight and spin-coated onto the graphene/Cu surface at 3000 rpm for 60 s. No solvent bakeout was performed. The graphene backside was removed, and the Cu was etched using the procedure described previously. The PC/graphene film was cleaned with the same modified RCA clean.[32] After transferring to SiO_2/Si and driving off residual water, the PC was removed by a sequence of three solvent baths: chloroform−acetone for 10 min, chloroform for 15 min, and acetone for 5 min. This produced clean graphene surfaces that did not require additional Ar/H_2 annealing.[33]

The graphene samples were next loaded in an AIXTRON 200/4 horizontal-flow, low-pressure MOCVD reactor for NW growth. Trimethyl-indium [TMI, $(CH_3)_3In$] and trimethyl-gallium [TMG, $(CH_3)_3Ga$] were employed as metal−organic precursors for the supply of group-III growth species, while arsine (AsH_3) was supplied as the hydride source for group-V species. Nanowire growths were carried out at reaction temperatures ranging between 520 and 580 °C, under a constant 7 $L \cdot min^{-1}$ flow of hydrogen (H_2) carrier gas, at a system pressure of 100 mbar. The flow of TMI and TMG precursors was modified in the ranges of 5.6−16 $\mu mol \cdot min^{-1}$ and 8.2−15.8 $\mu mol \cdot min^{-1}$, respectively, while AsH_3 flow rates were adjusted in different growths so as to maintain a V/III ratio range of 20 ± 1. All NW growths were terminated by the cessation of group-III precursor flows, at which point the samples were cooled from the growth temperature under a constant AsH_3 flow.

dx.doi.org/10.1021/nl304569d | Nano Lett. XXXX, XXX, XXX−XXX

Prior to NW growth, atomic force microscope (AFM) images were obtained using a Digital Instruments Dimension 3000 setup in tapping mode, for the evaluation of graphene layer location and thickness. The morphology, density, and orientation of the as-grown NW samples were inspected using an Hitachi S-4800 field-emission scanning electron microscope (FE-SEM). X-ray diffraction (XRD) experiments were performed on as-grown NW samples using a PANanalytical/Philips X'Pert MRD system. Raman scattering spectroscopy analysis of graphene samples was done, before and after NW growth, using a Renishaw inVia Raman microspectroscopy system, with excitation provided by a 632 nm wavelength laser line and a spatial resolution of approximately 2.5 μm. Sample preparation for analytical transmission electron microscopy (TEM) involved the ultrasonication of as-grown NW samples in a small volume of methanol, followed by the dispersal of the resultant NW-containing solution on lacey-carbon-coated Cu grids. A JEOL 2010F scanning transmission electron microscopy (STEM) system was used for all TEM experiments. Site-specific compositional analysis of NW heterostructures was carried out through high-angle annular dark-field (HAADF) imaging and energy dispersive X-ray (EDX) spectrometry using the JEOL 2010F microscope.

■ ASSOCIATED CONTENT

Ⓢ Supporting Information

Growth temperature dependences, growth along parasitic islands, linear defects, and edges of graphene films, InAs nanowire tip structure, distinguishing graphene-coated vs exposed-oxide regions, influence of the nanowire growth process on graphene substrate quality, growth of $In_xGa_{1-x}As$ NWs on graphene, growth evolution of InGaAs on graphene, and STEM analysis of short growth period InGaAs NWs. This material is available free of charge via the Internet at http://pubs.acs.org.

■ AUTHOR INFORMATION

Corresponding Author

*E-mail: xiuling@illinois.edu.

Notes

The authors declare no competing financial interest.

■ ACKNOWLEDGMENTS

P.K.M. gratefully acknowledges Dr. Gregor Lawson for insightful discussions. Financial support was provided in part by DOE under Award Numbers DEFG02-07ER46471 through the Frederick Seitz Materials Research Laboratory (P.K.M); the National Science Foundation DMR under Award # 1006581 (X.L.); the Air Force Office of Scientific Research (AFOSR) grant FA9550-10-1-0082 (E.P.), the Army Research Office (ARO) through the National Defense Science and Engineering Graduate Fellowship (J.D.W.), the Beckman Foundation (J.D.W.), the National Science Foundation (NSF) grant CHE 10-38015 (J.W.L.), and the Office of Naval Research (ONR) through grants N00014-10-1-0853 (A.B.). J.D.W. kindly acknowledges assistance in sample preparation by G. P. Doidge. TEM work was carried out in the Frederick Seitz Materials Research Laboratory Central Facilities, which are partially supported by the U.S. Department of Energy under grants DE-FG02-07ER46453 and DE-FG02-07ER46471.

■ REFERENCES

(1) Martensson, T.; Svensson, C. P. T.; Wacaser, B. A.; Larsson, M. W.; Seifert, W.; Deppert, K.; Gustafsson, A.; Wallenberg, L. R.; Samuelson, L. *Nano Lett.* **2004**, *4*, 1987.
(2) Bakkers, E. P. A. M.; van Dam, J. A.; De Franceschi, S.; Kouwenhoven, L. P.; Kaiser, M.; Verheijen, M.; Wondergem, H.; Van Der Sluis, P. *Nat. Mater.* **2004**, *3*, 769.
(3) Ihn, S.-G.; Song, J.-I. *Nano Lett.* **2007**, *7*, 39.
(4) Mohseni, P. K.; Maunders, C.; Botton, G. A.; LaPierre, R. R. *Nanotechnology* **2007**, *18*, 445304.
(5) Zervos, M.; Feiner, L.-F. *J. Appl. Phys.* **2004**, *95*, 281.
(6) Chuang, L. C.; Moewe, M.; Chase, C.; Kobayashi, N. P.; Chang-Hasnain, C. *Appl. Phys. Lett.* **2007**, *90*, 043115.
(7) Ertekin, E.; Greaney, P. A.; Chrzan, D. C.; Sands, T. D. *J. Appl. Phys.* **2005**, *97*, 114325.
(8) Hua, B.; Motohisa, J.; Kobayashi, Y.; Hara, S.; Fukui, T. *Nano Lett.* **2009**, *9*, 112.
(9) Qian, F.; Gradecak, S.; Li, Y.; Wen, C.-Y.; Lieber, C. M. *Nano Lett.* **2005**, *5*, 2287.
(10) Czaban, J. A..; Thompson, D. A.; LaPierre, R. R. *Nano Lett.* **2009**, *9*, 148.
(11) Colombo, C.; Heiß, M.; Gratzel, M.; Fontcuberta i Morral, A. *Appl. Phys. Lett.* **2009**, *94*, 173108.
(12) Svensson, C. P. T.; Martensson, T.; Tragardh, J.; Larsson, C.; Rask, M.; Hessman, D.; Samuelsson, L.; Ohlsson, J. *Nanotechnology* **2008**, *19*, 305201.
(13) Tomioka, K.; Motohisa, J.; Hara, S.; Hiruma, K.; Fukui, T. *Nano Lett.* **2010**, *10*, 1639.
(14) Shin, J. C.; Kim, K. H.; Yu, K. J.; Hu, H.; Yin, L.; Ning, C.-Z.; Rogers, J. A.; Zuo, J.-M.; Li, X. *Nano Lett.* **2011**, *11*, 4831.
(15) Shin, J. C.; Mohseni, P. K.; Yu, K. J.; Tomasulo, S.; Montgomery, K. H.; Lee, M. L.; Rogers, J. A.; Li, X. *ACS Nano* **2012**, *6*, 11074.
(16) Shin, J. C.; Choi, K. J.; Kim, D. Y.; Choi, W. J.; Li, X. *Crystal Growth and Design* **2012**, *12*, 2994.
(17) Dhaka, V.; Haggren, T.; Jussila, H.; Jiang, H.; Kauppinen, E.; Huhtio, T.; Sopanen, M.; Lipsanen, H. *Nano Lett.* **2012**, *12*, 1912.
(18) Mohseni, P. K.; Lawson, G.; Couteau, C.; Weihs, G.; Adronov, A.; LaPierre, R. R. *Nano Lett.* **2008**, *8*, 4075.
(19) Mohseni, P. K.; Lawson, G.; Adronov, A.; LaPierre, R. R. *IEEE J. Sel. Top. Quant.* **2011**, *17*, 1070.
(20) Tsakalakos, L.; Balch, J.; Fronheiser, J.; Korevaar, B. A.; Sulima, O.; Rand, J. *Appl. Phys. Lett.* **2007**, *91*, 233117.
(21) Nonoselov, K. S.; Geim, A. K.; Morozov, S. V.; Jiang, D.; Zhang, Y.; Dubonos, S. V.; Grigorieva, I. V.; Firsov, A. A. *Science* **2004**, *306*, 666.
(22) Schwierz, F. *Nat. Nanotechnol.* **2010**, *5*, 487.
(23) Bonoccorso, F.; Sun, Z.; Hasan, T.; Ferrari, A. C. *Nat. Photonics* **2010**, *4*, 611.
(24) Shi, Y.; Zhou, W.; Lu, A.-Y.; Fang, W.; Li, Y.-H.; Hsu, A. L.; Kim, S. M.; Kim, K. K.; Yang, H. Y.; Li, L.-J.; Idrobo, J.-C.; Kong, J. *Nano Lett.* **2012**, *12*, 2784.
(25) Wang, W.; Leung, K. K.; Fong, W. K.; Wang, S. F.; Hui, Y. Y.; Lau, S. P.; Chen, Z.; Shi, L. J.; Cao, C. B.; Surya, C. *J. Appl. Phys.* **2012**, *111*, 093520.
(26) Munshi, A. M.; Dheeraj, D. L.; Fauske, V. T.; Kim, D.-C.; van Helvoort, A. T. J.; Fimland, B.-O.; Weman, H. *Nano Lett.* **2012**, *12*, 4570.
(27) Kim, Y.-J.; Lee, J.-H.; Yi, G.-C. *Appl. Phys. Lett.* **2009**, *95*, 213101.
(28) Hong, Y. J.; Lee, W. H.; Wu, Y.; Ruoff, R.; Fukui, T. *Nano Lett.* **2012**, *12*, 1431.
(29) Koma, A. *Thin Solid Films* **1992**, *216*, 72.
(30) Wood, J. D.; Schmucker, S. W.; Lyons, A. S.; Pop, E.; Lyding, J. W. *Nano Lett.* **2011**, *11*, 4547.
(31) He, K. T.; Wood, J. D.; Doidge, G. P.; Pop, E.; Lyding, J. W. *Nano Lett.* **2012**, *12*, 2665.
(32) Liang, X.; Sperling, B. A.; Calizo, I.; Cheng, G.; Hacker, C. A.; Zhang, Q.; Obeng, Y.; Yan, K.; Peng, H.; Li, Q.; Zhu, X.; Yuan, H.;

Hight Walker, A. R.; Liu, Z.; Peng, L.-M.; Richter, C. A. *ACS Nano* **2011**, *5*, 9144.
(33) Lin, Y.-C.; Jin, C.; Lee, J.-C.; Jen, S.-F.; Suenaga, K.; Chiu, P.-W. *ACS Nano* **2011**, *5*, 2362.
(34) Hou, J. J.; Han, N.; Wang, F.; Xiu, F.; Yip, S. P.; Hui, A. T.; Hung, T. F.; Ho, J. C. *ACS Nano* **2012**, *6*, 3624.
(35) Jung, C. S.; Kim, H. S.; Jung, G. B.; Gong, K. J.; Cho, Y. J.; Jang, S. Y.; Kim, C. H.; Lee, C.-W.; Park, J. *J. Phys. Chem. C* **2011**, *115*, 7843.
(36) Regolin, I.; Sudfeld, D.; Luttjohann, S.; Khorenko, V.; Prost, W.; Kastner, J.; Dumpich, G.; Meier, C.; Lorke, A.; Tegude, F.-J. *J. Cryst. Growth* **2007**, *298*, 607.
(37) Hertenberger, S.; Funk, S.; Vizbaras, K.; Yadav, A.; Rudolph, D.; Becker, J.; Bolte, S.; Doblinger, M.; Bichler, M.; Scarpa, G.; Lugli, P.; Zardo, I.; Finley, J. J.; Amann, M.-C.; Abstreiter, G.; Koblmuller, G. *Appl. Phys. Lett.* **2012**, *101*, 043116.
(38) Guo, Y.-N.; Xi, H.-Y.; Auchterlonie, G. J.; Burgess, T.; Joyce, H. J.; Gao, Q.; Tan, H. H.; Jagadish, C.; Shu, H.-B.; Chen, X.-S.; Lu, W.; Kim, Y.; Zou, J. *Nano Lett.* **2013**, DOI: 10.1021/nl304237b.